The attached paper, "Dynamic Models of Fabry-Perot Interferometers," by David Redding, Martin Regehr, and Lisa Sievers, is in the final stages of preparation for submission to *Applied Optics*. We invite your comments prior to submission. Please direct your comments to any of the authors or to Albert Lazzarini (the Editorial Board Sponsor) prior to October 1, 1997.

Distributed by Stan Whitcomb 9/23/97

Distribution:
LIGO Science, LIGO Grads

cc:
Chronological File
Document Control Center

Dynamic Models of Fabry-Perot Interferometers

David Redding[*], Martin Regehr[†], Lisa Sievers[‡]

August 29, 1997

Abstract

Long-baseline, high-finesse Fabry-Perot interferometers can be used to make distance measurements that are precise enough to detect gravity waves. This level of sensitivity is achieved in part by dynamically isolating the interferometer mirrors, using pendulum mounts and high bandwidth cavity length control servos to reduce effects of seismic noise. This paper presents dynamical models of the cavity fields and signals of Fabry-Perot interferometers for use in designing and evaluating length control systems for gravity wave detectors. Models are described and compared with experimental data.

1. Introduction

Changes in the distance between the mirrors of a high-finesse Fabry-Perot interferometer can be measured to extraordinary precision through synchronous detection. This technique is used in various proposed methods for the broadband detection of gravitational radiation (Ref. 1). Fabry-Perot cavities used by the Laser Interferometer Gravity-Wave Observatory (LIGO) Project as gravity wave detector prototypes have demonstrated measurement sensitivities of 10^{-18} m/$\sqrt{Hz}$ at 200 Hz.

Successful operation of a Fabry-Perot cavity at this level of performance requires passive and active isolation of the optics from ambient seismic disturbances. The LIGO interferometer mirrors are hung from pendulum suspensions mounted on dynamically isolated platforms. The suspension system isolates the mirrors from seismically driven displacements at frequencies well above the pendulum resonant frequencies (common resonant frequency is 1 Hz). This passive isolation stage is augmented by lateral and longitudinal mirror position and angle control systems, as well as laser phase control. In this paper, we derive mathematical models for the longitudinal response of the cavity fields, assuming the cavity to be well aligned in angle.

The Pound-Drever-Hall (PDH) radio-frequency modulation technique (Ref. 2) provides signals for high-bandwidth mirror controls that "lock" the cavity length to the stabilized laser frequency. As sketched in Fig. 1, the laser light is phase modulated at RF before it enters the cavity. Light reflected back towards the laser is detected and synchronously demodulated. The in-phase demodulated signal is proportional to the phase difference between the carrier light incident on the cavity and the light reflected from the cavity, provided the cavity is within a fringe-width of resonance. This signal used by the control system to lock the cavity on resonance, as well as for length measurement.

---

[*] Principal Engineer, Jet Propulsion Laboratory, California Institute of Technology, Pasadena CA

[†] Staff Scientist, Ortel Corporation, 2015 Chestnut St., Alhambra CA

[‡] Senior Scientist, LIGO Project, California Institute of Technology, Pasadena CA

The control system must work in two operational modes. Initially the cavity will be out of resonance, having relatively large mirror velocities. The mirrors drift through the resonant condition, causing fringes to appear and disappear in the demodulated signals. During this initialization phase, a "Lock Acquisition" controller captures a fringe as it sweeps by, actuating the mirrors and source phase so as to establish the desired resonance condition.

Once the cavity is in resonance, the interferometer is placed in "Operations Mode," and the servos limit mirror deflections to a small fraction of a fringe, typically much less than 1 nanometer. The high cavity light levels that result enable the precise displacement measurements required for gravity wave detection.
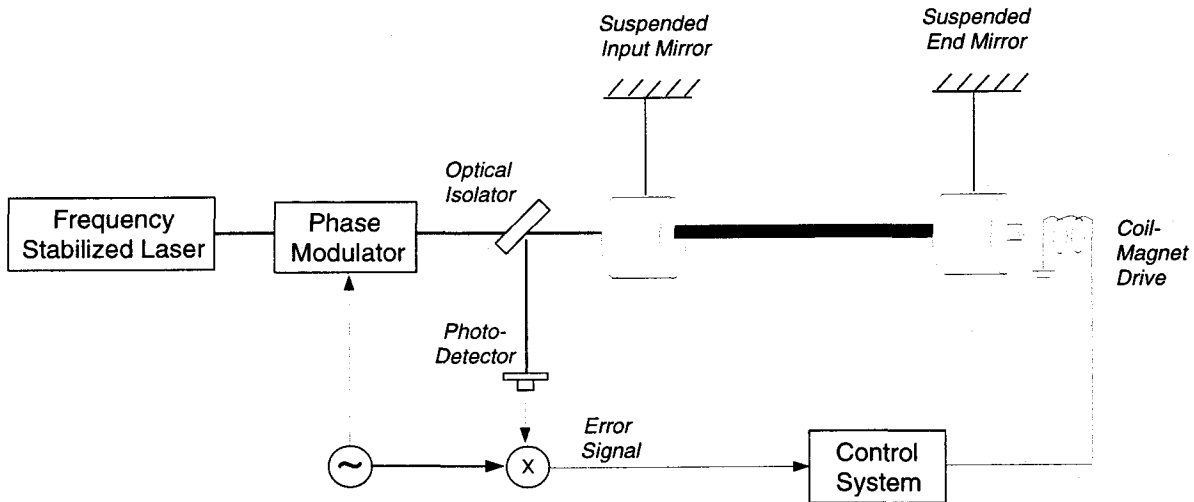

Figure 1. Fabry-Perot cavity and error signal generation.

The control problem is complicated by the fact that the cavity has significant dynamics. The long dwell time of the light in the cavity causes it to act as a temporal filter, with the detected field being a function of the cavity geometry and source phase at many previous times. In the Lock Acquisition regime, these dynamics are severely nonlinear. This fact notwithstanding, acquisition controllers have historically been based on linear small-signal linearized optical model.

Section 3 of this paper describes nonlinear optical models that accurately predict cavity signals at arbitrary displacement and velocity conditions. Cavity fields are governed by discrete time-difference equations, which may be reduced to differential equation form. Computer algorithms are discussed. Lock acquisition controllers designed using these models have demonstrated improved performance in hardware, compared to traditional designs (e.g., Ref. 3).

Section 4 of the paper derives linear models of the small-signal response of the cavity, for use in designing operations-mode servos. Two independent methods are used. The first approach linearizes the time-domain difference equations about the cavity resonant condition. The linearized equations are then Laplace-transformed to obtain analytic transfer functions from error signal to laser source phase and mirror motions. The second approach uses a direct frequency-response method, treating mirror and source

disturbances as audio-frequency oscillators, and directly computing the transfer functions from the static solution of the linearized cavity field equations.

Model validation was performed by comparing model predictions to experimental results, and by checking the consistency of the various models. The time-domain models were exercised in sine-sweep tests to reproduce the transfer functions computed by the 2 frequency-domain models, and all agree to numerical precision.

The modeling approaches presented here have proven invaluable for the design and analysis of controllers for LIGO interferometers, including Fabry-Perot and other, more complex interferometers as well. The models may be used for purposes other than control design, such as studies of noise effects on gravity wave detection.

2. Notation

In this paper we signify the complex transverse-electric field using the letter E. The point where the field is evaluated is indicated by a 2-letter subscript, as in E_{Aa}. The first subscript refers to the element in the beam train (here, to mirror A). The field is evaluated at an inertially-fixed point in the vicinity of the element, rather than on the moving surface of the element. The second subscript refers to the direction of the field: a to the field entering from the left; b to the field departing to the right; c to the field entering from the right; and d to the field departing to the left, as illustrated in Fig. 2.

When the cavity is illuminated by light at multiple frequencies, such as by the carrier and upper and lower sidebands that result from modulation of the source, an additional numeric subscript is used to signify the component of the field produced by illumination at each frequency. Thus E_{Aa0} denotes the input field at mirror A due to illumination at the carrier frequency, and E_{Aa1} and E_{Aa-1} denote the corresponding upper and lower sideband fields, respectively.

Properties of elements are identified using a single subscript, such as T_A and R_A for intensity transmittance and reflectance for mirror A. Lower case letters refer to amplitude transmittance and reflectance (i.e. $|r_A| = \sqrt{R_A}$). The sign used for the amplitude reflectance follows the Fresnel equations (Ref. 4); the negative value is used for light directly incident on the coated side of the mirror, and the positive value is used for light that comes through the substrate.

Finally, this work ignores transverse effects, such as mirror or beam tilt or beamwalk. The cavity is assumed to remain aligned in angle and to sustain only the TEM_{00} mode.
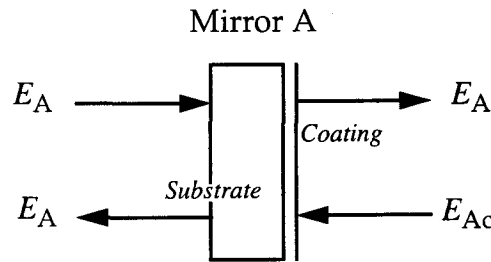
Mirror A

$E_A \longrightarrow$ $\longrightarrow E_A$

Coating

Substrate

$E_A \longleftarrow$ $\longleftarrow E_{Ac}$

Figure 2. Fields at a mirror.

3. Nonlinear Time Domain Models

3.1 Cavity Field Equations for a Single Frequency Source

The fields affected by a single stationary cavity mirror (mirror A) are illustrated in Fig. 2. The single frequency field incident on the left face of the mirror is labeled E_{Aa} and the field propagating to the right of the mirror is E_{Ab}. The field incident from the right is E_{Ac} and the field propagating to the left of the mirror is E_{Ad}. Summing the fields result in the following transmitted field expressions:

$$E_{Ab} = t_A E_{Aa} + r_A E_{Ac} \tag{EQ 1}$$

$$E_{Ad} = t_A E_{Ac} - r_A E_{Aa} \tag{EQ 2}$$

The power budget for each cavity mirror is such that:

$$R_A + T_A + A_A = 1 \tag{EQ 3}$$

where A_A is the power loss due to absorption and scattering.

As the mirror moves $\delta(t)$ (e.g. mirror driven by seismic background, control force, etc.) from its nominal inertially-fixed position, it imparts a phase shift on the reflected fields proportional to twice its displacement. Taking this into account, a more general expression of the fields at mirror A is

$$E_{Ab}(t) = t_A E_{Aa}(t) - r_A e^{2jk\delta_A(t)} E_{Ac}(t) \tag{EQ 4}$$

$$E_{Ad}(t) = t_A E_{Ac}(t) + r_A e^{-2jk\delta_A(t)} E_{Aa}(t) \tag{EQ 5}$$

The fields within a cavity consisting of 2 mirrors and a source are illustrated In Fig.3. The equations describing the fields are generated by applying Equations 4 and 5 to mirrors A and B, and by adding 2 additional equations defining the propagation between the 2 mirrors. For mirror B, assuming there is no illumination entering the back of the cavity ($E_{Bc} = 0$):

$$E_{Bb}(t) = t_B E_{Ba}(t) \tag{EQ 6}$$

$$E_{Bd}(t) = -r_B e^{-2jk\delta_B(t)} E_{Ba}(t) \tag{EQ 7}$$

The propagation over the distance L between the mirrors is:

$$E_{Ba}(t) = e^{-jkL} E_{Ab}(t - \tau) \tag{EQ 8}$$

$$E_{Ac}(t) = e^{-jkL} E_{Bd}(t - \tau) \tag{EQ 9}$$

Here $\tau = L/c$ is the light travel time between the two mirrors.

The input to the cavity comes from the laser source field, which can vary in phase and amplitude. Neglecting the distance between the source and the front mirror:

$$E_{Aa}(t) = t_{BS} E_S(t) \tag{EQ 10}$$

4

The field at the detector (neglecting the distance between the front mirror and the detector):

$$E_D(t) = r_{BS}E_{Ad}(t) \qquad \text{(EQ 11)}$$

The fields of primary interest are the circulating field E_{Ab} and the detector field E_D, from which the control signal is derived. Substituting among Equations 4-11, these can be expressed in terms of the source field and mirror displacement parameters. The field circulating in the cavity, sampled near the front mirror, is:

$$E_{Ab}(t) = t_A t_{BS}E_S(t) + g(t)E_{Ab}(t-2\tau) \qquad \text{(EQ 12)}$$

The "round trip gain," $g(t)$ is defined:

$$g(t) = r_A r_B e^{-2jk[L + \delta_B(t-\tau) - \delta_A(t)]} \qquad \text{(EQ 13)}$$

The field at the detector:

$$E_D(t) = r_A r_{BS}e^{-2jk\delta_A(t)}E_S(t) - t_A r_{BS}r_B e^{-2jk[L + \delta_B(t-\tau)]}E_{Ab}(t-2\tau) \qquad \text{(EQ 14)}$$
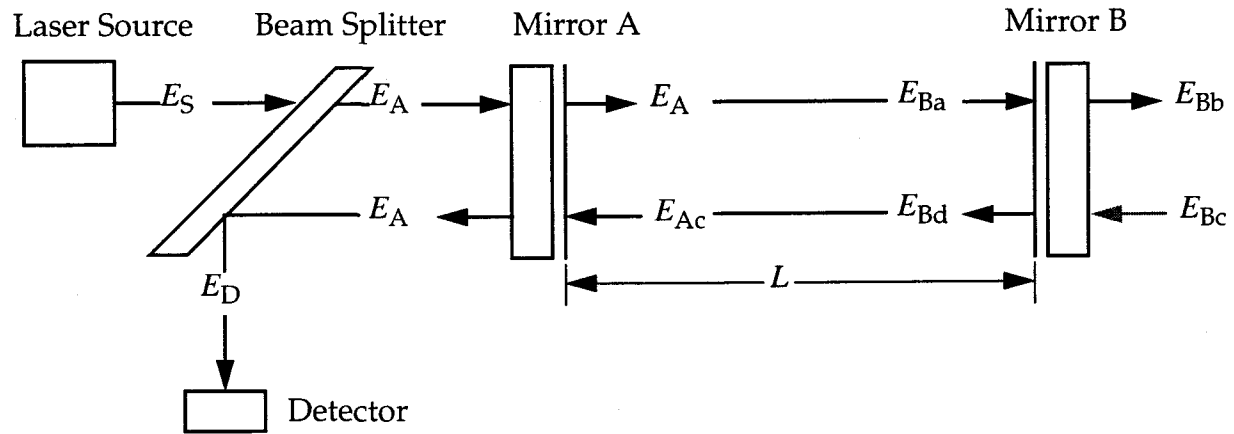

Figure 3. Fields in a Fabry-Perot Interferometer.

3.2 Static Response for a Single Frequency Source

In a static cavity, there is no variation in mirror position or source amplitude:

$$E_{Ab}(t) = E_{Ab}(t-2\tau) \equiv E_{Ab} \qquad \text{(EQ 15)}$$

$$E_S(t) = E_S(t-2\tau) \equiv E_S \qquad \text{(EQ 16)}$$

$$\delta_A(t) = \delta_A(t-2\tau) \equiv \delta_A \qquad \text{(EQ 17)}$$

$$\delta_B(t-\tau) = \delta_B(t-3\tau) \equiv \delta_B \qquad \text{(EQ 18)}$$

Substituting Equations 15-18 into Equation 12 and simplifying, the static-cavity circulating field is:

$$E_{Ab} = \frac{t_A t_{BS} E_S}{1 - r_A r_B e^{-2jk(L + \delta_B - \delta_A)}} \qquad \text{(EQ 19)}$$

Similarly, the detector field is:

$$E_D = \left[r_A r_{BS} e^{-2jk\delta_A} - \frac{t_A^2 t_{BS} r_{BS} r_B e^{-2jk[L + \delta_B]}}{1 - r_A r_B e^{-2jk(L + \delta_B - \delta_A)}} \right] E_S \qquad \text{(EQ 20)}$$

These are standard results appearing in textbooks (e.g., Ref. 5).

3.3 Time Response for a Single Frequency Source

In a dynamically-varying cavity, the source and mirror states will change as arbitrary functions of time. The output of the cavity at a time t is computed from the cavity field difference equations (Equations 12-14), given the (single-frequency) source field at time t, the cavity mirror displacements at time t (mirror A) and $t - \tau$ (mirror B), and the circulating field at time $t - 2\tau$. Of course, the circulating field at time $t - 2\tau$ is a function of the source at time $t - 2\tau$, cavity mirror displacements at time $t - 2\tau$ and $t - 3\tau$, and the circulating field at time $t - 4\tau$, which is itself a function of the circulating field at time $t - 4\tau$, cavity mirror displacements at time $t - 4\tau$ and $t - 5\tau$, and the circulating field at time $t - 6\tau$, and so on (see Fig. 4).

This recursive sequence continues back in time until the cavity was first turned on. As a practical matter, though, it is not always necessary to go that far back in time. There is a finite number of beams (n_{beams}) that must be summed to achieve a specific level of accuracy in the calculation of the circulating field, as illustrated in Fig. 4. If the cavity geometry is fixed at the resonance, which is the most sensitive condition, the circulating field can be written:

$$E_{Ab} = \frac{t_A t_{BS} E_S}{1 - r_A r_B} = t_A t_{BS} E_S \left[\sum_{i=1}^{n} (r_A r_B)^i + \frac{(r_A r_B)^{n+1}}{1 - r_A r_B} \right] \qquad \text{(EQ 21)}$$

Here n is the number of beams explicitly summed. The normalized error due to summing a finite number of beams is ε, where:

$$\varepsilon = \frac{t_A t_{BS} E_S \dfrac{(r_A r_B)^{n+1}}{1 - r_A r_B}}{E_{Ab}} = (r_A r_B)^{n+1} \qquad \text{(EQ 22)}$$

The error level ε can be specified (e.g., 0.1% of the full resonant circulating field). The minimum number of summed beams n_{beams} that gives residual error less than ε is:

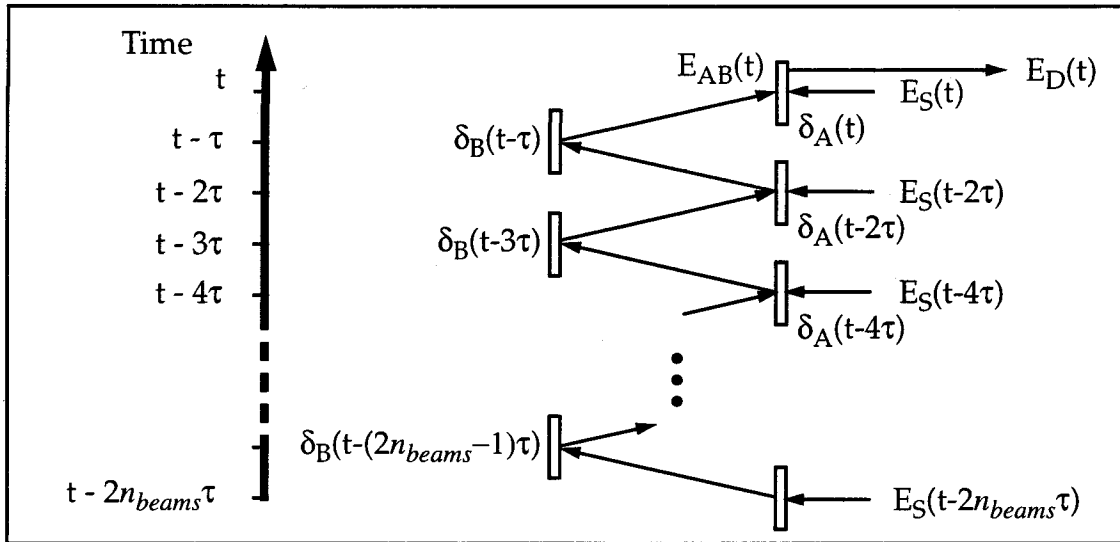$$n_{beams} = \frac{\log \varepsilon}{\log r_A r_B} - 1 \qquad \text{(EQ 23)}$$

Figure 4. Dependence of cavity fields on past cavity history.

Assuming that the one-way cavity light time τ remains constant, the full computation for the circulating field can be written:

$$E_{Ab}(t) = t_A t_{BS} E_S(t) + g(t)(t_A t_{BS} E_S(t - 2\tau) + \tag{EQ 24}$$
$$g(t - 2\tau)(t_A t_{BS} E_S(t - 4\tau) +$$
$$g(t - 4\tau)(\ldots(t_A t_{BS} E_S(t - (2(n - 1)\tau)) +$$
$$g(t - 2n\tau)(t_A t_{BS} E_S(t - 2n\tau)))\ldots)))$$

A simple algorithm that realizes this calculation as part of a time simulation is summarized in pseudo-code in Fig. 5.

```
EAb = tA*Es                              ! Initial circulating field
for time = 0 to t by 2*tau,              ! Begin simulation time loop
   call dynamics (delA,delB,ES,time)     ! Compute cavity geometry
   g = rA*rB*exp(-2*j*k*(L + delB - delA) ! Compute round-trip cavity gain
   EAb = tBS*tA*Es + g*EAb               ! Update circulating field
   if (mod(time,dtprint)=0),
      call print (EAb,delA,delB,dLs,time) ! Print state at times of interest
   end;
end;                                     ! End simulation time loop
```

Figure 5. Cavity simulation algorithm for time scales less than $n_{beams}\tau$.

The computational effort required by this algorithm per one-way light time τ is quite small. It is a good approach for high-finesse cavities driven by high-bandwidth controllers, where the time interval of interest (dtprint) is less than $n_{beams}\tau$.

The algorithm of Fig. 5 may not be the fastest for modeling lower-finesse cavities, or low-bandwidth controls. For cases where the shortest time interval of interest is longer than $n_{beams}\tau$, it is more efficient to reorder the calculation. Equation 24 is rewritten:

$$E_{Ab}(t) = t_A t_{BS} \left[E_S(t) + \sum_{n=1}^{n_{beams}} \left(\prod_{i=0}^{n} g(t-2i\tau) \right) E_S(t-2n\tau) \right] \qquad \text{(EQ 25)}$$

This approach limits the number of beams that must be evaluated to n_{beams}. The algorithm of Fig. 6. illustrates its implementation in pseudo-code.

```
for time = 0 to t by dtprint,                   ! Begin simulation time loop
    call dynamics (delA,delB,Es,time)           ! Compute cavity geometry
    gprod = 1                                   ! Initialize running gain product
    EAb = tBS*tA*Es                             ! Initialize circulating field sum
    for n = 1 to nbeams                         ! Loop to evaluate sum
        loopTime = time-2*n*tau                 ! loopTime runs backwards from time
        call dynamics (delA,delB,Es,loopTime)   ! Compute cavity geometry
        g = rA*rB*exp(-2*j*k*(L + delB - delA)  ! Compute round-trip cavity gain
        gprod=g*gprod                           ! Update running product
        EAb = EAb + gprod*tBS*tA*ES             ! Update circulating field sum
    end;
    call print (EAb,delA,delB,dLs,time)         ! Print state at times of interest
end;                                            ! End simulation time loop
```

Figure 6. Cavity simulation algorithm for time scales greater than $n_{beams}\tau$.

Equation 25 can be viewed as a Green's function solution for the cavity fields. The product in parentheses is the impulse response of the circulating field at time t to the source field at the time $t - 2n\tau$. The sum is then the convolution of the impulse response with the source field at all relevant past times (all n less than n_{beams}). This ordering of the calculation is also used in later sections, in the derivation of transfer functions.

The models of Equations 24 and 25 neglect second-order effects of deviations from the nominal one-way light time τ. These occur when the mirrors are displaced from their nominal positions ($\delta \neq 0$), so that the beams arrive at the mirrors at slightly different times than assumed by the model. For mirror displacements of a few wavelengths, this time-of-arrival error is about 10^{-16} seconds per traversal of the cavity. In very high-finesse cavities, this might grow to about 10^{-12} seconds total after many bounces. The neglected beam phase is equal to this time-of-arrival error times the velocity of the mirror, which is typically less than a few wavelengths per second for Lock Acquisition (much less in Operation Mode). The ratio of this worst-case error to the width of the fringe is about 1 part per million for a cavity with a finesse of 15,000, and much smaller for lower-finesse cavities and/or smaller velocities. This level of error is usually negligible.

3.4 Approximate Differential Equation Form for the Cavity Field Equations

The cavity field difference equations can easily be converted to an approximate differential-equation form. The resulting continuous-time equations may result in faster simulation times for some interferometers, though at the possible cost of some accuracy. They are also convenient for modal analysis.

Before converting, it is convenient to introduce a new state $F(t)$, which is the value of the circulating field at the previous round trip of the light:

$$F(t) = E_{Ab}(t - 2\tau) \qquad \text{(EQ 26)}$$

The field equation (Eq. 12) becomes a first state equation:

$$E_{Ab}(t) = t_A t_{BS} E_S(t) + g(t)F(t) \qquad \text{(EQ 27)}$$

The Laplace transform of $F(t)$ is the following:

$$F(s) = e^{-2\tau s} E_{Ab}(s) \qquad \text{(EQ 28)}$$

The delay e^{-2ts} can be approximated by a rational function, such as one of the Pade approximants. The *(m,n)* Pade approximant is a rational function with m zeroes and n poles such that the first $m+n$ terms in the Taylor series of this function are the same as the first $m+n$ terms of the Taylor series expansion of e^{-2ts}. For example, the Taylor series expansion of e^{-2ts} is:

$$e^{-2\tau s} = 1 - 2\tau s + (2\tau s)^2 - \dots \qquad \text{(EQ 29)}$$

The 0,1 pade approximant takes the form $1/(1 + a\,s)$ (with a to be determined), which has Taylor series expansion $1/(1 + a\,s) = 1 - as + \dots$ Matching coefficients for the first 2 terms, the *(0,1)* Pade approximant is:

$$e^{-2\tau s} \cong \frac{1}{1 + 2\tau s} \qquad \text{(EQ 30)}$$

Substituting into Eq. 28:

$$F(s) = \frac{1}{1 + 2\tau s} E_{Ab}(s) \qquad \text{(EQ 31)}$$

This expression can now be transformed back into the time domain to form a second state equation:

$$F(t) = E_{Ab}(t) + 2\tau \frac{d}{dt} F(t) \qquad \text{(EQ 32)}$$

Here it is seen that the (0,1) Pade approximates the past value of $E_{Ab}(t)$ by extrapolating linearly back in time. The state equations can be rewritten in standard form. Differentiating Eq. 27 and substituting between Eqs. 27 and 32:

$$\frac{d}{dt} E_{Ab}(t) = \frac{1}{2\tau} [(g(t) - 1)F(t) + t_A t_{BS} E_S(t)] + t_A t_{BS} \frac{d}{dt} E_S(t) + F(t) \frac{d}{dt} g(t) \qquad \text{(EQ 33)}$$

$$\frac{d}{dt} F(t) = \frac{1}{2\tau} (E_{Ab}(t) - F(t)) \qquad \text{(EQ 34)}$$

These equations form a system of differential equations to replace the time-difference field equation (Eq. 12) in evaluating the cavity fields.

The approximation that has been introduced is that the circulating field changes only linearly in the time it takes the light to traverse the cavity twice. Higher-order approximants, or other higher-order approximations such as a Taylor series expansion, can be used in cases where the fields change nonlinearly. Such higher-order approximations replace Eq. 34. In general they are written in standard state-space form,

in terms of a multiple-element state vector $\vec{x}(t)$. The elements of $\vec{x}(t)$ are linear combinations of higher-order derivatives of $E_{Ab}(t)$, $E_S(t)$, $g(t)$ and $F(t)$, which provide a better basis for extrapolation. The general form for the time-delay equations is:

$$\frac{d}{dt}\vec{x}(t) = A \cdot \vec{x}(t) + B \cdot E_{AB}(t) \qquad \text{(EQ 35)}$$

$$F(t) = C \cdot \vec{x}(t) + D \cdot E_{AB}(t) \qquad \text{(EQ 36)}$$

Combining these equations with Eq. 27 and eliminating $F(t)$:

$$\frac{d}{dt}\vec{x}(t) = \left[\frac{A + BCg(t)}{1 - Dg(t)}\right] \cdot \vec{x}(t) + \left[\frac{Bt_A t_{BS}}{1 - Dg(t)}\right] \cdot E_s(t) \qquad \text{(EQ 37)}$$

$$E_{AB}(t) = \frac{1}{1 - Dg(t)}[g(t)C \cdot \vec{x}(t) + t_A t_{BS} \cdot E_S(t)] \qquad \text{(EQ 38)}$$

For the (m,n) Pade approximant, A is an nxn matrix, and B and C are of dimension $nx1$ and $1xn$ respectively. These can be solved algebraically, as in the case above. Alternatively, commercially available control system design software provides functions that automatically transform the poles and zeroes of the Pade approximant transfer functions to the time-domain matrices A, B, C, and D, making it easy to generate differential field equations of any desired order. The cavity fields are then solved by integrating Eqs. 37 and 38.

The differential equation model introduces some error through the time-delay approximations described above. To estimate the magnitude of this error, and to determine the Pade order necessary for good accuracy in the case of a slow open-loop drift through a resonance, a simple test was performed. Successive simulations were run by integrating the differential field equations forward in time, then increasing the order of the Pade approximant and repeating. The order was increased until no changes in the results occured with further increase in order. The (0,1) and (1,1) Pade approximants produced slightly different results, and the (1,1) results were indistinguishable from all higher-order results. Of course, stability of the result with increasing order in one case is not a guarantee of accuracy in all cases. For simulations involving rapid field changes, the difference-equation form is preferred, as it is free of these errors.

3.5 Time Response Example: Single Frequency Source

Figure 7 shows the carrier field intensity in a Fabry-Perot cavity as the input mirror (Mirror A) sweeps through the resonance condition (which occurs at $\delta = 0$). The full dynamic response of the cavity, computed by integrating the Equation 12, is shown as the solid line. The static response, which neglects the dynamics of the cavity, as per Equation 19, is shown as the dashed line.

As shown in Fig. 7, the passage of the mirror through the resonance condition causes a bolt of high amplitude light to build up in the cavity. After the cavity passes through the fringe, this light dissipates gradually, while bouncing from mirror to mirror. The frequency of the light is shifted higher with each successive bounce, creating a Doppler "chirp." The parameters defining this example are listed in Table 1. The width of the

10

resonant fringe is 0.11 nanometers, about 0.02% of the wavelength. The lock acquisition controller must stabilize the mirror over a time period much shorter than the duration of the "chirp" signal (see Ref. 3).
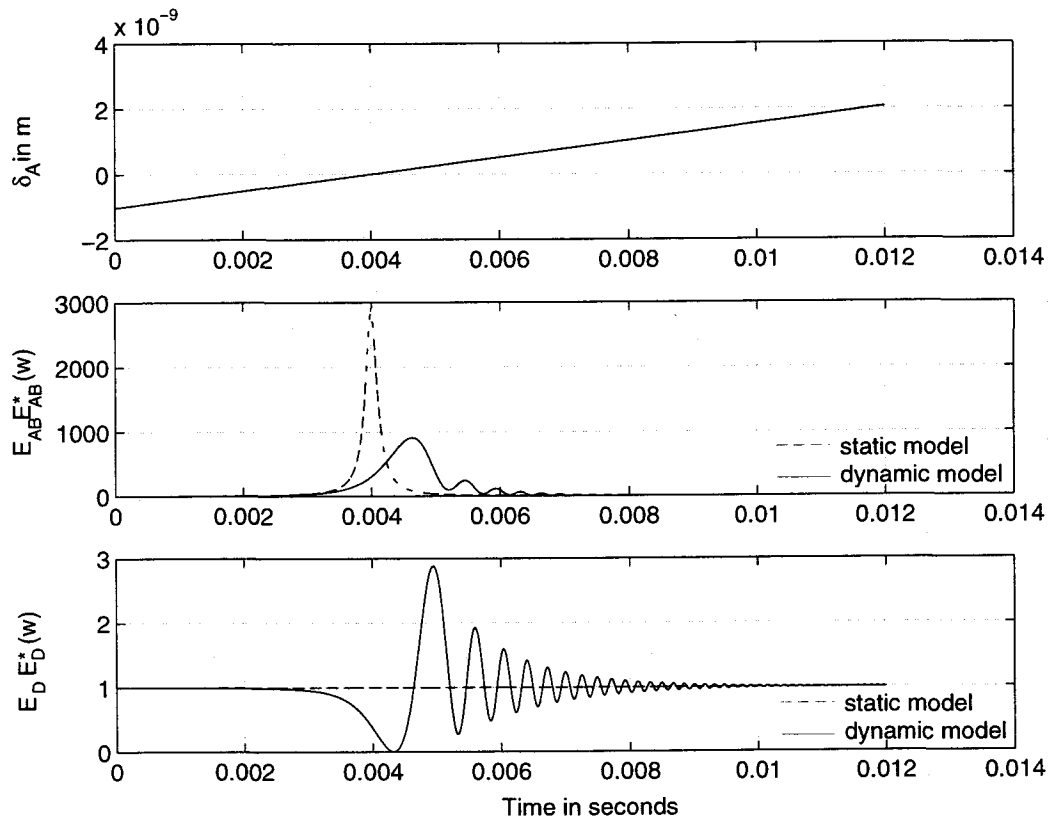

Figure 7. Field intensities as the cavity goes through resonance.

Table 1: Example parameters for 40-meter interferometer.

Parameter	Value	Parameter	Value
RA	0.998604	Wavelength	0.5145 μm
RB	1	Mirror A velocity	0.25 μm/sec
Length	40 m	Finesse	4500

3.6 Demodulated Cavity Phase Signals

Radio-frequency phase modulation and synchronous detection provides a means of creating signals that are proportional to the phase of the reflected field, provided that the cavity is near resonance. Phase modulation is implemented using a Pockels cell in the beam immediately prior to the cavity (Fig. 1). The (radio) frequency f_{mod} of the

modulation is chosen so that the resulting sidebands are out-of-resonance in the cavity, preferably anti-resonant, so only a minimum of sideband field leaks into the cavity.

For small modulation depth Γ at frequency $f_{mod} = \omega_{mod}/2\pi$, the field after the modulator (the cavity source field) is written in terms of Bessel functions as (Ref. 5):

$$E_S(t) = E_{laser}(t)(J_0(\Gamma) + J_1(\Gamma)e^{j\omega_{mod}t} - J_1(\Gamma)e^{-j\omega_{mod}t})e^{j\omega_0 t} + \text{higher order terms} \quad \text{(EQ 39)}$$

Here the laser frequency is $f_0 = \omega_0/2\pi = c/\lambda_0$. The source field can be rewritten as the sum of 3 independent fields of slightly different color:

$$E_S(t) = E_{S0}(t)e^{j\omega_0 t} + E_{S1}(t)e^{j\omega_1 t} - E_{S-1}(t)e^{-j\omega_{-1}t} \quad \text{(EQ 40)}$$

The carrier and sideband source fields are:

$$E_{S0}(t) = E_{laser}(t)J_0(\Gamma) \quad \text{(EQ 41)}$$

$$E_{S1}(t) = E_{laser}(t)J_1(\Gamma) \quad \text{(EQ 42)}$$

$$E_{S-1}(t) = -E_{laser}(t)J_1(\Gamma) \quad \text{(EQ 43)}$$

The carrier wavelength is the source laser wavelength, and the upper and lower sidebands have slightly longer and shorter wavelengths, respectively. The wavelengths for the upper and lower sidebands are as follows:

$$\lambda_{\pm 1} = 2\pi c/(\omega_0 \mp \omega_{mod}) = (2\pi c)/\omega_{\pm 1} \quad \text{(EQ 44)}$$

The nominal operational condition of the cavity makes the carrier resonant in the cavity by making the nominal cavity length, L_{nom}, an integer multiple of half the carrier wavelength:

$$L_{nom} = n(\lambda_0/2) \quad \text{where n= integer} \quad \text{(EQ 45)}$$

The modulation frequency is then chosen to make the sidebands approximately anti-resonant when the carrier is resonant, by choosing the modulation wavelength close to an integer factor n_{mod} of $4L_{nom}$.

$$f_{mod} = (c/\lambda_{mod}) \cong n_{mod}(c/(4L)) \quad \text{(EQ 46)}$$

If it is chosen to be exactly antiresonant then the second order sidebands are also resonant in the arm, causing the interferometer response to be more complicated. For the above choice of modulation frequency, the effective phase of each sideband is then shifted approximately ±90° per round-trip of the cavity, relative to the carrier. Relative to the other sideband, the shift is 180°. The choice of integer n_{mod} determines the particular modulation frequency. For long cavities a relatively large number may be desirable to reduce the effects of $1/f$ noise in the detection.

The detector field of the cavity at a time t can be computed separately for each frequency component, by application of Equations 12 and 14 to the source fields of Equations 41-43. The total detector field is simply the sum of the detector fields at each frequency:

$$E_D(t) = E_{D0}(t)e^{j\omega_0 t} + E_{D1}(t)e^{j\omega_1 t} - E_{D-1}(t)e^{-j\omega_{-1}t} \quad \text{(EQ 47)}$$

12

The detector intensity is the modulus squared of the field of Equation 47. It includes terms at DC, frequencies at f_{mod} and $2f_{mod}$, as well as higher harmonics. The error signal for the control system is the output of the demodulator which is synchronous with the modulation signal at f_{mod}. With sinusoidal modulation, the demodulated in-phase signal I_{In} is:

$$I_{In} = 2Imag(E_{D0}(t)(E^*_{D-1}(t) - E^*_{D1}(t)))$$ (EQ 48)

The quadrature-phase signal I_{quad} is:

$$I_{Quad} = 2Real(E_{D0}(t)(E^*_{D-1}(t) + E^*_{D1}(t)))$$ (EQ 49)

3.7 Time Response Examples: Cavity Phase Signals

Two examples are discussed in this section. The first continues the example of Fig. 7. Figure 8 shows the demodulated in-phase and quadrature phase signals detected at the input mirror for the cavity defined in Table 1 as the mirrors swing through the carrier resonance. Modulation frequency was 12.5 MHz, which puts the sidebands in an antiresonant condition in the cavity as per Equation 45.
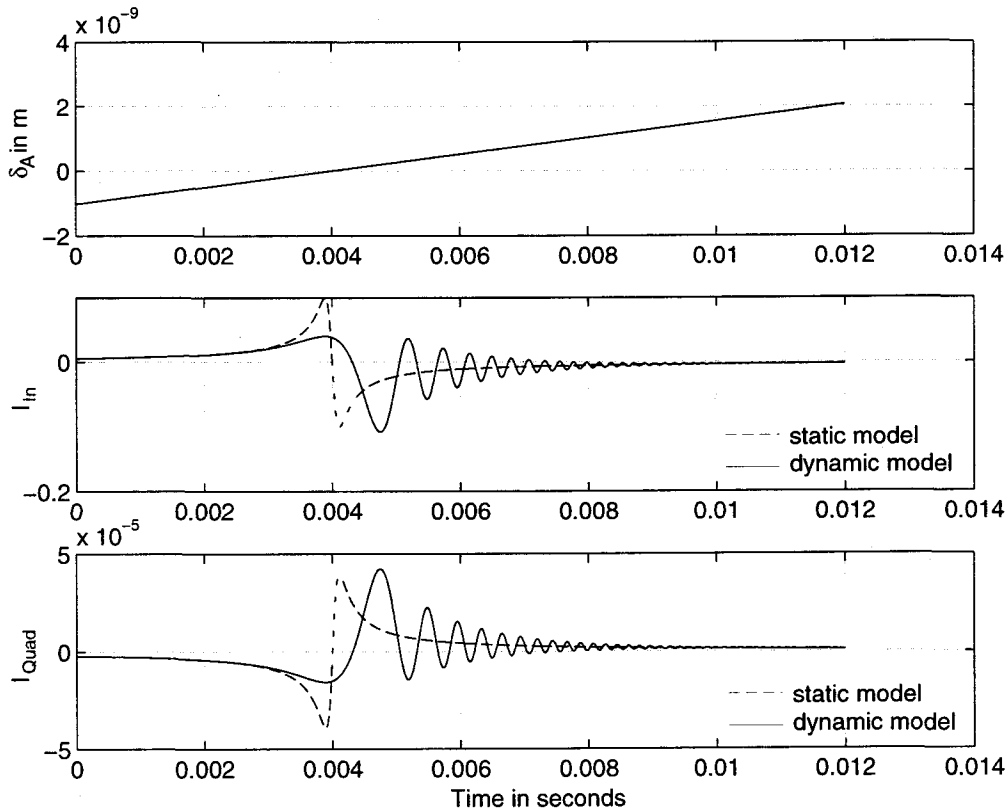

Figure 8. Constant velocity sweep showing signals at input mirror detector.

The second example compares simulated and experimental response data for the LIGO 40 m interferometer (Ref. 1). This interferometer provides an experimental testbed for

13

development of gravity wave detectors. In the configuration we ran, the interferometer is made up of two orthogonal suspended 40 m Fabry-Perot cavities. Both cavities have a finesse of 15000 with an approximate storage time (amplitude half life) of 0.338 milliseconds. The main function of one of the cavities is to provide a reference for stabilizing the laser frequency to approximately $10^{-6} \, Hz/\sqrt{Hz}$. We used the second cavity to measure the optical response to mirror motion. The interferometer and signal extraction scheme is shown in Fig. 1. Experimental time traces were taken of the error signal (i.e. demodulated in-phase signal at the input mirror) as the cavity mirrors swung freely through resonance; a characteristic trace is shown in Fig. 9.
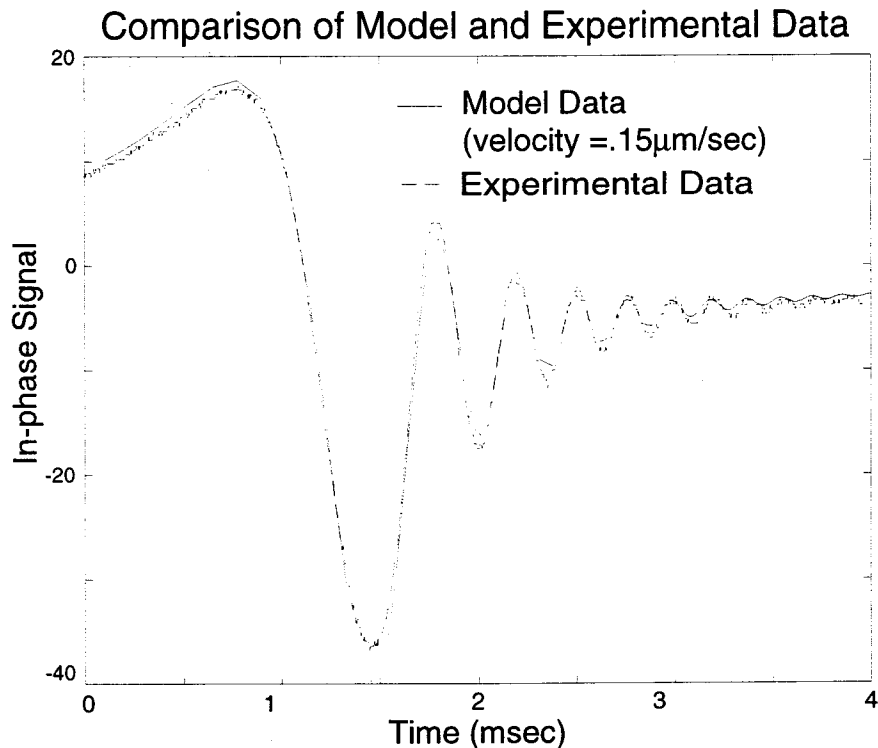
Comparison of Model and Experimental Data

Figure 9. Measured and predicted control system error signal (In-phase demodulated signal) as cavity goes through resonance at a constant velocity.

To compare the experimental data with model data we fit two parameters: the relative velocity of the cavity test masses; and the absolute amplitude of the field incident on the photodetector. This is necessary as we have no independent means of measuring these parameters. Figure 9 compares model and experimental response for a typical case, showing good agreement.

4. Linear Frequency Domain Models

4.1 Response of Interferometer Near Resonance

In order to use a Fabry-Perot interferometer as a Gravity Wave Detector, the length of the interferometer must be controlled so that the carrier field in the cavity resonates (i.e. the

relative position between the mirrors is kept at $n\lambda_0/2$) for long periods of time. When the interferometer is close to the resonant state the interferometer can be modeled as a simple linear system. A linear model is important for two reasons: 1) it provides a predictive model for how gravity wave strain drives the error signal in Operations Mode and 2) it provides a simple transfer function model that can be used as an element for both the Operations Mode and Acquisition mode control system design.

We can obtain optical models for small motions of the cavity mirrors and source phase about the resonant condition in 3 distinct ways. The first approach, described in this section, reduces the solution of the in-phase demodulated signal (Equation 48) to the case of small disturbances, and then takes the Laplace transform to obtain cavity transfer functions in closed form. The second approach uses a direct frequency-response method, treating mirror or source disturbances as audio-frequency modulation and numerically generating transfer functions from the small-motion equations. This approach was also pursued by Weiss (Ref. 8). A third approach is simply to exercise the nonlinear time-domain model in a series of single-frequency sine sweeps, recording amplitude and phase response at each frequency, to build up a complete transfer function. The sine sweep method provides a useful cross-check of the time-domain and frequency-domain models and represents what is actually done experimentally. A comparison of the 3 methods produce essentially identical results.

4.2   Frequency Response Model Derivation by Laplace Transform

Assuming that the cavity is near its ideal configuration, so that the carrier is resonant and the sidebands are essentially anti-resonant, the cavity gain factors for the carrier and sidebands (Eq. 13) become:

$$g_0(t) = r_A r_B e^{-2jk[\delta_B(t-\tau)-\delta_A(t)]} \tag{EQ 50}$$

$$g_1(t) = g_{-1}(t) = -r_A r_B e^{-2jk[\delta_B(t-\tau)-\delta_A(t)]} \tag{EQ 51}$$

where δ_A and δ_B are mirror displacements of mirror A and B, respectively. Assume also that the magnitude of the laser illumination is constant. The source field is then written (for the carrier):

$$E_{S0}(t) = E_{s0} e^{-jk\delta_s} \tag{EQ 52}$$

Carrier source amplitude E_{s0} is a constant; similar expressions can be obtained for the sidebands. To further simplify the equations, we introduce a cumulative beam phase parameter Δ_n, where:

$$\Delta_n(t) = 2\sum_{i=1}^{n} \delta_B(t-(2i-1)\tau) - 2\sum_{i=1}^{n} \delta_A(t-2i\tau) + \delta_s(t-2n\tau) \tag{EQ 53}$$

We also introduce 2 cavity reflectance parameters R_g and R_r:

$$R_g = r_A r_B \tag{EQ 54}$$

$$R_r = \frac{t_A^2 t_{BS} r_{BS}}{r_A} \qquad \text{(EQ 55)}$$

Substituting and simplifying, the detected carrier field becomes:

$$E_{D0}(t) = \left[r_A e^{-jk(2\delta_A(t) + \delta_s(t))} + R_r \sum_{n=1}^{n_{beams}} [R_g^{\ n} e^{-jk\Delta_n(t)}] \right] E_{s0} \qquad \text{(EQ 56)}$$

Similarly, the difference of the detected sideband fields becomes:

$$E_{D\text{-}1}(t) - E_{D1}(t) = 2\left[r_A e^{-jk(2\delta_A(t) + \delta_s(t))} + R_r \sum_{n=1}^{n_{beams}} [(-R_g)^n e^{-jk\Delta_n(t)}] \right] E_{s1} \qquad \text{(EQ 57)}$$

In these equations we neglect the very small differences between the wave numbers k of the sidebands and carrier, using the carrier value for all terms. Multiplying the carrier and sideband terms to obtain the demodulated in-phase signal (Equation 48):

$$\begin{aligned}
I_{In}(t) = 4E_{s0}E_{s1}\mathrm{Imag}\Bigg(& r_A^2 - r_A^2 R_r^2 \sum_{n=1}^{n_{beams}} [R_g^{\ n} e^{-jk(\Delta_n(t) - 2\delta_A(t) - \delta_s(t))}] \\
& - r_A^2 R_r^2 \sum_{n=1}^{n_{beams}} [(-R_g)^n e^{-jk(\Delta_n(t) - 2\delta_A(t) - \delta_s(t))}] \\
& + R_r^4 \left[\sum_{n=1}^{n_{beams}} R_g^{\ n} e^{-jk\Delta_n(t)} \right]\left[\sum_{n=1}^{n_{beams}} (-R_g)^n e^{jk\Delta_n(t)} \right] \Bigg)
\end{aligned} \qquad \text{(EQ 58)}$$

Near resonance, the phasor exponentials can be replaced with the first 2 terms in a power series expansion:

$$\begin{aligned}
I_{In}(t) = 4E_{s0}E_{s1}\mathrm{Imag}\Bigg(& r_A^2 - r_A^2 R_r^2 \sum_{n=1}^{n_{beams}} [R_g^{\ n}(1 - jk(\Delta_n(t) - 2\delta_A(t) - \delta_s(t)))] \\
& - r_A^2 R_r^2 \sum_{n=1}^{n_{beams}} [(-R_g)^n(1 - jk(\Delta_n(t) - 2\delta_A(t) - \delta_s(t)))] \\
& + R_r^4 \left[\sum_{n=1}^{n_{beams}} R_g^{\ n}(1 - jk(\Delta_n(t))) \right]\left[\sum_{n=1}^{n_{beams}} (-R_g)^n(1 - jk(\Delta_n(t))) \right] \Bigg)
\end{aligned} \qquad \text{(EQ 59)}$$

Constant terms can be extracted from the sums, and some sums can be closed using the binomial theorem. The result is:

$$I_{In}(t) = 4E_{s0}E_{s1}\left(-R_r^2\left[\frac{R_g}{1-R_g}(2\delta_A(t)+\delta_s(t)) + \sum_{n=1}^{n_{beams}}[R_g{}^n\Delta_n(t)]\right]\right.$$

$$-R_r^2\left[\frac{R_g}{1+R_g}(2\delta_A(t)+\delta_s(t)) - \sum_{n=1}^{n_{beams}}[(-R_g)^n\Delta_n(t)]\right]$$

$$\left.+R_r^4\left[\frac{R_g}{1-R_g}\sum_{n=1}^{n_{beams}}(-R_g)^n\Delta_n(t) + \frac{R_g}{1+R_g}\sum_{n=1}^{n_{beams}}R_g{}^n\Delta_n(t)\right]\right) \qquad \text{(EQ 60)}$$

The above expression can be written explicitly in terms of the source phase and mirror position states by substituting for the cumulative beam phase parameter Δ_n from Eq. 54 into Eq. 60.

The transfer functions of the demodulated in-phase signals are obtained by taking the Laplace transform of Eq. 60 and closing the sums. The transfer function from source phase to in-phase demodulated signal is:

$$\frac{I_{In}}{\delta_s}(s) = 4kE_{s0}E_{s1}\left(\frac{-2R_g}{1-R_g^2} + \left(1 - t_A^2 r_A^2\frac{R_g}{1-R_g}\right)\frac{R_g e^{-2\tau s}}{1+R_g e^{-2\tau s}}\right.$$

$$\left.+ \left(1 + t_A^2 r_A^2\frac{R_g}{1+R_g}\right)\frac{R_g e^{-2\tau s}}{1-R_g e^{-2\tau s}}\right) \qquad \text{(EQ 61)}$$

The transfer function from mirror A displacement to in-phase demodulated signal is:

$$\frac{I_{In}(s)}{\delta_A} = 8kE_{s0}E_{s1}\left(\frac{-2R_g}{1-R_g^2} + \left(\frac{-1}{1+R_g} + t_A^2 r_A^2\frac{R_g}{1-R_g^2}\right)\frac{R_g e^{-2\tau s}}{1+R_g e^{-2\tau s}}\right.$$

$$\left.+ \left(\frac{1}{1-R_g} + t_A^2 r_A^2\frac{R_g}{1-R_g^2}\right)\frac{R_g e^{-2\tau s}}{1-R_g e^{-2\tau s}}\right) \qquad \text{(EQ 62)}$$

The transfer function from mirror B to in-phase demodulated signal is:

$$\frac{I_{In}}{\delta_B}(s) = 8kE_{s0}E_{s1}\left(\left(\frac{1}{1+R_g} - t_A^2 r_A^2\frac{R_g}{1-R_g^2}\right)\frac{R_g e^{-\tau s}}{1+R_g e^{-2\tau s}}\right.$$

$$\left.-\left(\left(\frac{1}{1-R_g} + t_A^2 r_A^2\frac{R_g}{1-R_g^2}\right)\frac{R_g e^{-\tau s}}{1-R_g e^{-2\tau s}}\right)\right) \qquad \text{(EQ 63)}$$

4.3 Cavity Transfer Functions in Rational Form

These transfer functions can be further simplified by eliminating certain sideband terms (which do not affect the response significantly at frequencies below half a free spectral range) and replacing the time-delay exponentials ($e^{-2\tau s}$) with a rational approximation.

The resulting rational transfer functions provide a good match to the exact form over the main frequency band of interest and offer a convenient form for control design.

As before, the time delay can be approximated as a truncated infinite series, derived by picking a form for the solution, expanding it out in MacLaurin series, and matching coefficients of terms of like order to the series expansion of $e^{-2\tau s}$. We picked a form that matches the high-frequency response well. The result is:

$$e^{-2\tau s} = -\frac{(s-\sigma)(s-(\sigma \pm j\omega))(s-(\sigma \pm 2j\omega))\ldots}{(s+\sigma)(s+(\sigma \pm j\omega))(s+(\sigma \pm 2j\omega))\ldots} \qquad \text{(EQ 64)}$$

Here (in Hz.):

$$\sigma = \frac{\pi}{2\tau} \qquad \text{(EQ 65)}$$

$$\omega = \frac{\pi}{\tau} \qquad \text{(EQ 66)}$$

Experience suggests that, in truncating the series, one should carry all terms up to twice the highest frequency of interest. The rational transfer functions in normalized form are as follows.

$$\frac{I_{In}}{\delta_A}(s) = \frac{(s+\sigma)\prod\limits_{n=1}^{\infty}(s+\sigma+jn\omega)\prod\limits_{n=1}^{\infty}(s+\sigma-jn\omega)}{(s+\alpha)\prod\limits_{n=1}^{\infty}(s+\alpha+j2\omega)\prod\limits_{n=1}^{\infty}(s+\alpha-j2\omega)} \qquad \text{(EQ 67)}$$

$$\frac{I_{In}}{\delta_B}(s) = \frac{I_{In}}{\delta_A}(s)\frac{(s-2\sigma)\prod\limits_{n=1}^{\infty}(s-2\sigma+j2(2n-1)\omega)\prod\limits_{n=1}^{\infty}(s+2\sigma-j2(2n-1)\omega)}{(s+2\sigma)\prod\limits_{n=1}^{\infty}(s+2\sigma+j2(2n-1)\omega)\prod\limits_{n=1}^{\infty}(s+2\sigma-j2(2n-1)\omega)} \qquad \text{(EQ 68)}$$

where $\alpha=-\log(r_A r_B)/(2\tau)$. The first few poles and zeros of these transfer functions are sketched in Fig. 10.
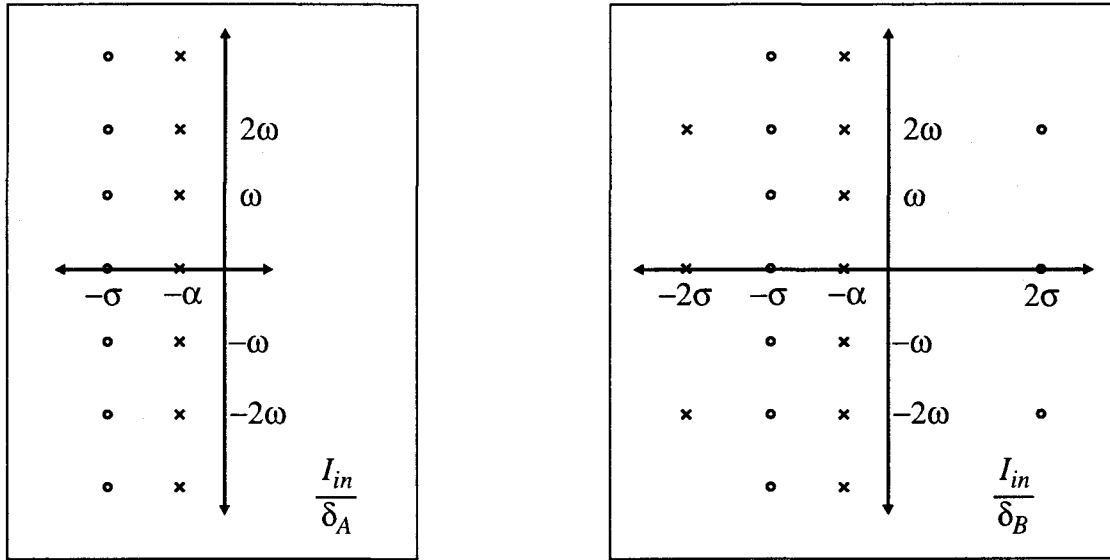
Figure 10. Roots of the cavity mirror transfer functions (rational approximation).

4.4   Linear Model Derivation by Direct Frequency Response

This section presents a second method for computing the same transfer functions. We take the point of view that a moving mirror phase-modulates the light reflected from it, and thereby imposes phase-modulation sidebands on this light. Consider (for example) mirror B to be moving with small amplitude X at frequency ω_B in an otherwise stationary cavity:

$$\delta_B(t) \;=\; X\cos\omega t \;=\; \mathrm{Real}(Xe^{i\omega_B t}) \tag{EQ 69}$$

The mirror motion frequency ω_B is in the audio band, as opposed to the RF frequencies ω_{mod} used in the PDH detection ($\omega_B \ll \omega_{mod}$). The light reflected from the mirror is then phase modulated. From Eq. 40:

$$E_{Bd}(t) \;=\; -r_B(1 - jkXe^{j\omega_B t} + jkXe^{-j\omega_B t})E_{Ba}(t) \tag{EQ 70}$$

Here we have used equation (39) with the approximations $J_0(2kX) \approx 1$ and $J_1(2kX) \approx kX$. We call the sidebands imparted to the light by reflection from a moving mirror "audio" sidebands, since the frequencies of interest are typically audio frequencies, and to distinguish them from the RF sidebands described earlier. If the light incident on the mirror has been radio-frequency phase modulated then each of the RF sidebands will also have a pair of audio sidebands imposed on it.

At this point it is convenient to modify our notation by adding a second numeric subscript to the field variables to index the audio sidebands. For example $E_{Bd1\text{-}1}$ is the amplitude of the lower audio sideband of the upper RF sideband. Now suppose that the light incident on mirror B contains 9 frequencies; the carrier and two RF sidebands, and a pair of audio sidebands on each of those three frequencies. Then the total field incident on mirror B is written:

$$E_{Ba} = \sum_{u=-1}^{1} \sum_{v=-1}^{1} E_{Bauv} e^{-i(u\omega_{mod} + v\omega_B)t} \qquad \text{(EQ 71)}$$

Now assume that the moving mirror is the only source of audio sidebands so that their amplitude is proportional to X. Then substituting into Eq. (67) and discarding terms quadratic in X we obtain:

$$E_{Bd} = -r_B \sum_{u=-1}^{1} \left(E_{Bau0} e^{-iu\omega_{mod}t} + \sum_{v=-1,1} (E_{Bauv} + ikXE_{Bau0}) e^{-i(u\omega_{mod} + v\omega_B)t} \right) \qquad \text{(EQ 72)}$$

By discarding terms quadratic in X we are neglecting two effects which are significant for larger-amplitude mirror motion. One is the creation of additional frequencies when audio sidebands are imposed on audio sidebands, and the other is the attenuation of the carrier and RF sidebands by such audio sidebands which fall back on the carrier or RF sidebands.

From Eq. 72 we see that the carrier and RF sidebands are reflected from the moving mirror in the same way as they would be were the mirror stationary, but the amplitude of each audio sideband is changed by the amount $ikXE_{Bau0}$. The moving mirror behaves like a source of light at the frequencies of the audio sidebands.

Now we can solve for the response of the interferometer to mirror motion in two stages. First we compute the static fields from Eqs. 1, 2 and 4 through 11, substituting Eq. 71 for Eq. 40, to get the amplitudes of the audio sidebands. Then the demodulated signal is computed following Eqs. 48 and 49. Only terms at frequencies $\omega_B + \omega_{mod}$ and $\omega_B - \omega_{mod}$ are of interest. With sinusoidal modulation, the in-phase response is:

$$I_{In} = 2Real\left\{ \sum_{u=-1}^{0} \sum_{v=-1}^{0} (E^*_{Bauv} E_{Ba(u+1)(v+1)} + E_{Bau(v+1)} E^*_{Ba(u+1)v}) \right\} \qquad \text{(EQ 73)}$$

The quadrature phase response is:

$$I_{Quad} = 2Real\left\{ \sum_{u=-1}^{0} \sum_{v=-1}^{0} (E^*_{Bauv} E_{Ba(u+1)(v+1)} - E_{Bau(v+1)} E^*_{Ba(u+1)v}) \right\} \qquad \text{(EQ 74)}$$

These expressions are the transfer functions from mirror B motion to detected in-phase and quadrature-phase signals, at an excitation frequency ω_B, for comparison with those derived earlier. A similar analysis leads to transfer functions for motion of mirror A and source phase.

In practice all of the above manipulations are performed by a computer program which uses data specifying mirror reflectances, transmittances and relative locations to construct a matrix corresponding to the set of linear equations to be solved, and then solves the linear system once for each of the nine frequencies of interest. Once the amplitude at the photodetector of the light at each of these nine frequencies is known, the demodulated signal is computed. The process is repeated for a sequence of different excitation frequencies to develop the full transfer functions.

This method of numerical analysis is easily extended to other optical configurations, such as systems containing more than two mirrors or beam splitters. The computer program accommodates additional optical elements by increasing the dimensions of the matrix relating the optical fields. This approach is elaborated in more detail in Ref. 7.

4.5 Frequency Response Example

A very long-baseline interferometer, typical of the lengths used for LIGO gravity-wave detection, provides an example to illustrate frequency response characteristics. Interferometer parameters are summarized in Table 2. Figure 11 shows the transfer function from source phase to in-phase demodulated voltage. There is a zero at DC, indicating that low-frequency changes in the source phase have little or no effect on the in-phase signal. The gain increases with frequency, saturating above 90 dB for frequencies above the cavity pole at 92.4 Hz. There are sharp dips in the amplitude response at frequencies that are multiples of half the cavity free spectral range. These occur when the excitation becomes synchronous or anti-synchronous with the carrier light circulating in the cavity, aliasing the DC condition (0 gain) in the first case, and killing the leaked light contribution to the detector field in the second.

Table 2: Example parameters for 4 km interferometer.

Parameter	Value	Parameter	Value
RA	0.9699	Finesse	410
RB	0.9998	Free Spectral Range	37.5 kHz
Length	4,000 m	Cavity pole frequency	92.4 Hz
Wavelength	0.5145 μm	Fringe width	2.5 nm

The transfer functions from motion of mirrors A and B to in-phase demodulated voltage are shown in Figs. 12 and 13, respectively. The amplitude response is identical for both mirrors. The gain is flat at frequencies below the cavity pole and then rolls off as f^{-1}. At high frequencies, there are peaks in the amplitude response occurring at multiples of the cavity free spectral range, where the mirror motion is synchronous with the light circulating in the cavity. This effectively aliases the DC condition, so the peaks recover the DC gain value. There are also very narrow zeros at odd multiples of half the free spectral range, where the excitation is anti-synchronous with the circulating carrier field (and synchronous with the sideband fields). Although the amplitude response of the two transfer functions is identical, the phase response is different. The difference is a time delay whose time constant is the one-way light travel time in the cavity. These plots were generated using Method 1; they are indistinguishable from those generated using Method 2.
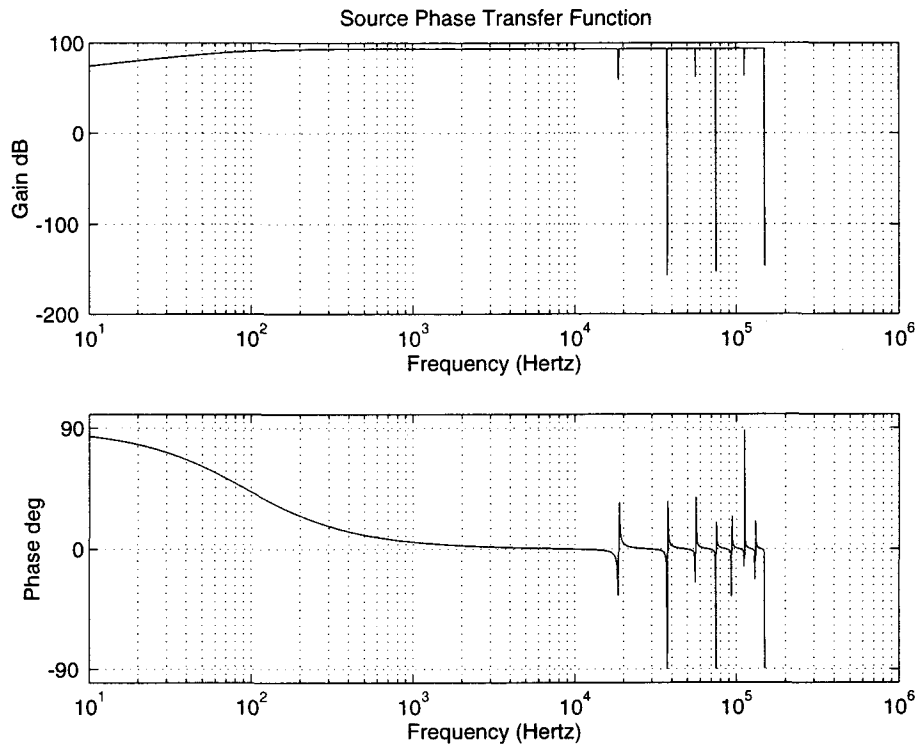
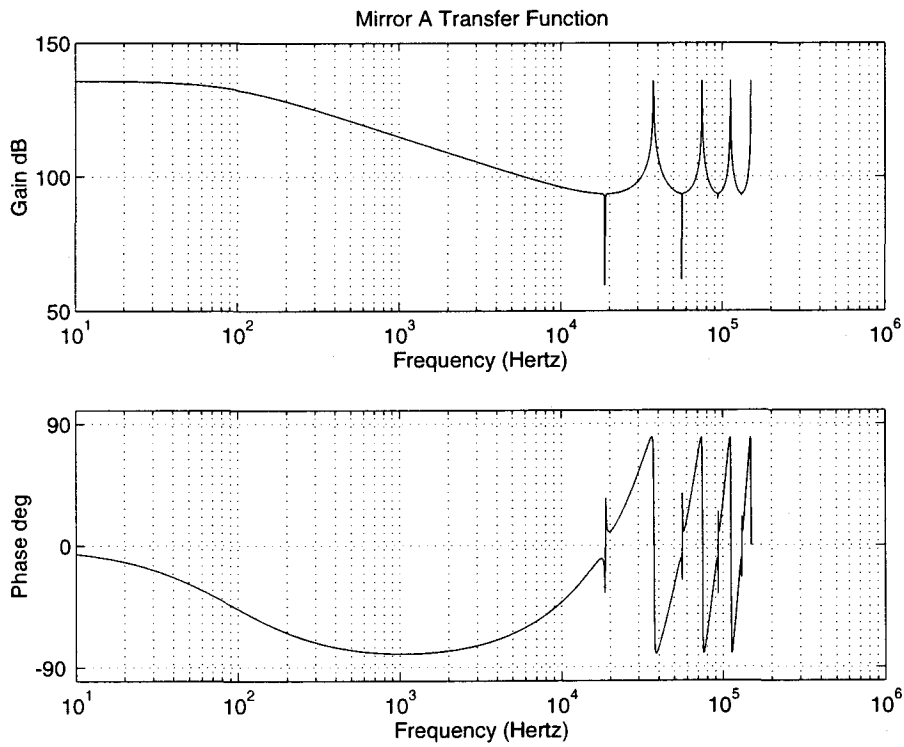**Figure 11. Source phase transfer function example.**

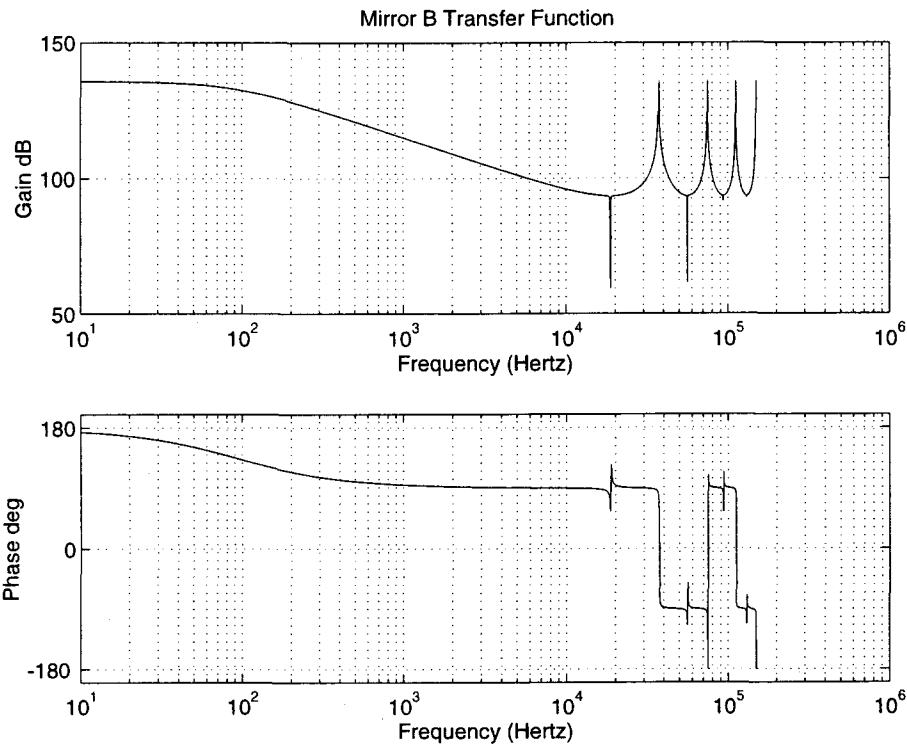**Figure 12. Mirror A transfer function example.**

22

Figure 13. Mirror B transfer function example.

5.   Conclusion

The models presented here capture the longitudinal dynamics of the light circulating in well-aligned Fabry-Perot cavities, for large or small displacements of mirrors or source phase. The models provide useful tools for the design of both linear and acquistion mode cavity length controls. They are also useful for computing the influence of laser phase and mirror seismic noise effects on the noise performance of cavity length measurements. The same basic modeling approach can be extended to encompass more complex interferometer configurations, higher-order modes, and different modulation schemes.

6.   Acknowledgements

The authors wish to thank Stan Whitcomb, Hiro Yamamoto and Jordan Camp of Caltech for their contributions to this work. Thanks also to Rai Weiss of MIT for useful discussions.

7.   References

1. A. Abramovici et al, *Science* , Vol. 256, pp. 281-284, April 17, 1992.

2. R. Drever, J. Hall, F. Kowalski, J. Hough, G. Ford, A. Munley and H. Ward, "Laser Phase and Frequency Stabilization Using an Optical Resonator," *Applied Physics B*, Vol. 31, pgs. 97-105, 1983.

3. J. Camp, L. Sievers, R. Bork and J. Heefner, "Guided Lock Acquisition in a Suspended Fabry-Perot Cavity," *Optics Letters*, Vol. 20, No. 24, pp. 2463-2465, Dec 15, 1995.

4. M. Born and E. Wolfe, <u>Principles of Optics</u>, Pergamon Press, 1987.

5. A. Siegman, <u>Lasers</u>, University Science Books, 1986.

6. G. Franklin, J. Powell and A. Emami-Naeini, *Feedback Control of Dynamic Systems*, Addison-Wesley, 1994.

7. M. Regehr, <u>Signal Extraction and Control for an Interferometric Gravitational Wave Detector</u>, Ph.D. Thesis, California Institute of Technology, Pasadena, California, 1995.